Enabling Real-Time Imaging and Onboard RFI Localization for Three-Level Quantized Microwave Interferometric Radiometers

Ziyang Zhang , Hao Liu * , Donghao Han , Xing Tong , Hao Lu , Changxing Huo

Posted Date: 27 March 2026

doi: 10.20944/preprints202603.2178.v1

Keywords: real-time imaging; correlation coefficients estimation; three-level quantization; RFI localization

Article

Enabling Real-Time Imaging and Onboard RFI Localization for Three-Level Quantized Microwave Interferometric Radiometers

Ziyang Zhang [1,2], Hao Liu [1,*], Donghao Han [1], Xing Tong [1], Hao Lu [1] and Changxing Huo [1]

[1] The Key Laboratory of Microwave Remote Sensing, National Space Science Center, Chinese Academy of Sciences, Beijing 100190, China

[2] The School of Electronic, Electrical and Communication, University of Chinese Academy of Sciences, Beijing 10049, China

* Correspondence: liuhao@mirslab.cn

Highlights

What are the main findings?

- Real-time brightness temperature (BT) reconstruction for microwave interferometric radiometers (MIRs) is achieved through the development of fast estimation algorithms for the normalized three-level quantization threshold.
- An onboard real-time data processing framework is established for three-level quantization MIRs, enabling real-time BT imaging and radio frequency interference (RFI) localization based on the real-time reconstructed BT images.

What is the implication of the main finding?

- Microwave interferometric radiometers with real-time imaging capability can significantly improve in-orbit intelligent observation performance, particularly for onboard RFI processing, information extraction and fusion. This also enables new application scenarios such as alternative vision under degraded visual environments (DVE).

Abstract

Real-time imaging processing of microwave interferometric radiometer (MIR) has great potential in various application field, such as onboard data processing, onboard information fusion and alternative visual application. The primary challenge lies in the computational complexity of the entire processing chain, including both visibility function pre-processing and brightness temperature (TB) reconstruction. In this study, the real-time estimation of the normalized threshold level is identified as the key step for enabling re-al-time imaging of three-level quantized MIR system. Three algorithms - Acklam's algorithm (AKA), polynomial fitting algorithm (PFA), and Taylor expansion algorithm (TEA) - are proposed and evaluated. The PFA shows balanced performance in terms of estimation accuracy and computation efficiency. Leveraging the proposed algorithms, this paper further establishes an onboard real-time processing framework for three-level quantization MIRs, enabling real-time TB imaging and RFI localization. A real-time imaging experiment has been carried out with a 15-element, 50GHz one-dimensional MIR system, which successfully realizes real-time imaging of fast-moving vehicles on the expressway with greatly reduced computational latency (an imaging time of 570.9μs for 159 baselines). A further flight experiment employing an L-band system verifies the feasibility of onboard RFI localization and achieves a localization accuracy within 2.1% of the spatial resolution.

Keywords: real-time imaging; correlation coefficients estimation; three-level quantization; RFI localization

 doi:10.20944/preprints202603.2178.v1

1. Introduction

Microwave interferometric radiometry, also known as synthetic aperture radiometry, was originally developed in the field of radio astronomy in early 1960's, and then introduced in the field of earth observation in 1980's in the context of spaceborne L-band mission concept for soil moisture and ocean salinity measurement [1].

Microwave interferometric radiometer (MIR) obtains the cross-correlations of all pairs of antennas in the thinned array. Considering the huge amount of real-time calculation, the cross-correlations are usually realized by low-level quantized digital correlator [2], which is a core functional unit of an interferometric radiometer [3]. For example, the Soil Moisture and Ocean Salinity (SMOS) mission employs the simplified 1-bit/2-level quantization scheme, in which the quantization operation of a receiving channel can be readily implemented using a single comparator [4]. In contrast, three-level quantization is realized with a pair of symmetric positive and negative threshold comparators. Compared with 1-bit quantization, it preserves amplitude information and has been increasingly adopted in practical MIR systems [5,6]. The brightness temperature (TB) distribution within the field of view (FOV) can be reconstructed with all these correlation outputs based on Fourier Transform. This TB reconstruction process is usually done offline and not belong to the function of the radiometer system itself. An important reason is that mapping raw low-level quantized correlation counts to true correlation values is needed before TB reconstruction. This mapping procedure is nonlinear, and its real-time implementation is usually incompatible with the constraints of space-borne hardware resources [7].

In recent years, onboard data processing has emerged as a promising solution to ad-dress the challenge of enhancing in-orbit intelligent observation capability, reducing downlink data rate and data latency [8]. More specifically for spaceborne passive micro-wave remote sensing, onboard radio frequency interference (RFI) detection and mitigation is gradually becoming a necessary and standard capability for current and future micro-wave radiometers [9–13]. The NASA Soil Moisture Active Passive (SMAP) mission firstly designed and implemented onboard calculations of receiving signal's spectrograms and statistical parameters (e.g., kurtosis), thereby preserving sufficient information for RFI detection, mitigation, and localization in ground segment [14]. The CubeSat Radiometer Radio Frequency Interference Technology (CubeRRT) mission conducted tests for onboard RFI detection and filtering, aiming to explore the feasibility of reducing the raw downlink data volume [15]. Both aforementioned efforts were based on traditional real-aperture radiometer systems. In the Chinese Ocean Salinity Mission (COSM), Microwave Imager Combined Active and Passive (MICAP) achieved the first onboard RFI detection and mitigation for its L-band 1D synthetic aperture radiometer [11]. However, the onboard RFI filtering also resulted in the loss of RFI positional information, preventing subsequent on-ground localization of the interferences. Onboard real-time imaging processing will not only offer an alternative approach for RFI detection and mitigation, but also enable the possibility of simultaneous, onboard real-time RFI localization, which is the key information need to be preserved and reported to national administrations and the ITU for further regulatory activities [16].

Real-time passive microwave imaging also has great potential in other various ap-plication fields [17]. It can serve as an alternative vision option under degraded visual environments (DVE), especially under the condition with fog, smoke, haze, sandstorm, etc. [18] It has also been utilized for personnel security check purpose, especially at milli-meter-wave frequency range, with its unique capability which can penetrate clothing and reveal concealed threats or contrabands [19]. Most of these real-time imaging systems are based on focal plane imaging [20], only a few experimental systems are based on interferometric imaging [21].

In brief, real-time passive microwave interferometric imaging can play important roles in onboard data processing, information fusion and alternative vision applications. Developing resource-efficient real-time imaging technology suitable for high-integration hardware platforms, based on low-level quantized cross-correlation, can facilitate the above applications.

 doi:10.20944/preprints202603.2178.v1

The paper is organized as follows. Section 2 identifies the calculation of the normalized threshold level as the key step for achieving real-time TB reconstruction within a three-level quantized digital correlation architecture. Based on the existing onboard digital processing system architecture of the MICAP L-band one-dimensional synthetic aperture radiometer, a comprehensive digital processing system architecture is proposed, which integrates digital correlation, RFI detection and mitigation, real-time TB reconstruction, and RFI localization. Section 3 presents fast threshold estimation algorithms and an RFI localization algorithm suitable for the aforementioned processing system architecture and field programmable gate array (FPGA) computational resources. Section 4 validates the real-time TB imaging and RFI localization using two 1D synthetic aperture radiometer prototypes. Finally, Section 5 concludes the paper.

2. Integrated Architecture for Real-time Processing: Bottleneck Analysis and System Design

This section established the theoretical foundation and the proposed system architecture for real-time imaging and RFI localization. First, Part A introduces the three-level quantized MIR and identifies the normalized threshold level estimation as the critical computational bottleneck. Part B then explains the fundamental necessity of performing onboard RFI localization prior to data mitigation. Based on these theoretical constraints and functional requirements, Part C presents a highly integrated digital processing architecture that inherently enables both real-time TB reconstruction and RFI localization simultaneously within a unified FPGA platform.

2.1. Real-Time Brightness Temperature Reconstruction

According to the Corbella equation [22], the relationship between TB and visibility function (VF) can be written as below

$$V_{ij}(u,v) = \frac{\sqrt{D_i D_j}}{4\pi} \iint\limits_{\xi^2+\eta^2\le 1} \frac{T_B(\xi,\eta) - T_r}{\sqrt{1-\xi^2-\eta^2}} F_{ni}(\xi,\eta)\, F_{nj}^{*}(\xi,\eta) \cdot \tilde{r}_{ij}\left(-\frac{u\xi+v\eta}{f_0}\right) e^{-j2\pi(u\xi+v\eta)}\, d\xi d\eta \tag{1}$$

where D_i and D_j are antenna directivities, T_B is brightness temperature, T_r is physical temperature of the receiver, $F_{ni}(\xi,\eta)$ and $F_{nj}(\xi,\eta)$ are the normalized antenna voltage patterns, $\tilde{r}_{ij}\left(-\frac{u\xi+v\eta}{f_0}\right)$ is the so-called fringe washing function.

In the real MIR system, the calibrated visibility function is normally converted from the raw output counts of the digital correlator. Figure 1 illustrates the data processing architecture of a three-level quantized MIR, using the MICAP L-band 1-D MIR as an example [11]. In this framework, signal quantizer, correlator, and RFI detection and mitigation are implemented onboard. The correlation data after RFI mitigating are downlinked to ground station for correlation coefficients calculation and TB reconstruction.

 doi:10.20944/preprints202603.2178.v1

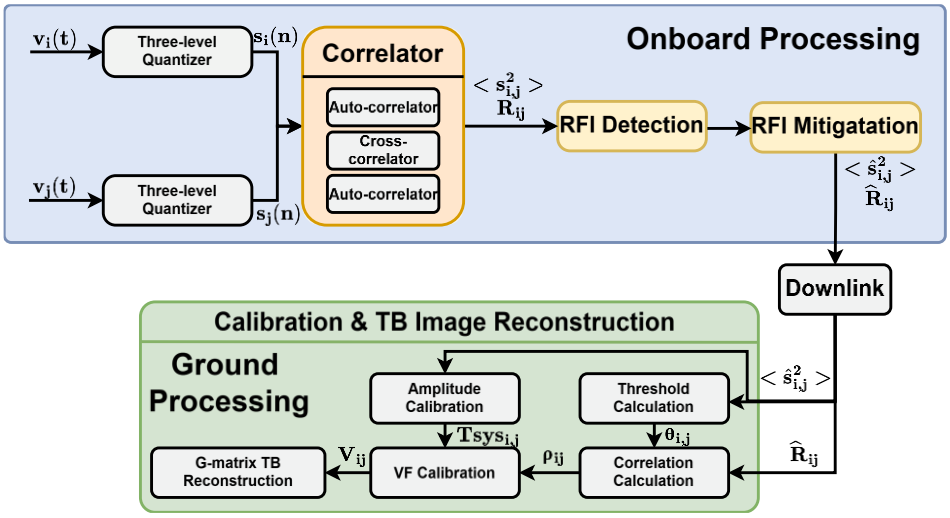

Figure 1. Architecture of three-level quantized MIR with onboard RFI detection and mitigation.

The transfer function of three-level quantizer in Figure 1 is as follows:

$$s(n) = \begin{cases} 1, \text{if } v > v_{th} \\ -1, \text{if } v < -v_{th} \\ 0, \text{otherwise} \end{cases} \tag{2}$$

The quantized signals $s(n)$ from all receiver channels undergo correlation and integration within the correlator to derive the digital variance $< s_{i,j}^2 >$ of individual channels and the digital covariance R_{ij} between channel pairs. The RFI-mitigated correlation data are accumulated over an extended integration period to generate the output $< \hat{s}_{i,j}^2 >, \hat{R}_{ij}$, which are subsequently downlinked to the ground station.

Due to limited onboard computational resource, processing steps shown in Figure 1 such as estimating correlation coefficients ρ_{ij} from the three-level samples and reconstructing TB are performed on the ground. According to Price's theory [7], correlation coefficient can be calculated using the following equation:

$$\begin{gathered} \rho_{ij} = \frac{1}{c_1} R_{ij} - \frac{c_3}{c_1^4} R_{ij}^3 + \left(3\frac{c_3^2}{c_1^7} - \frac{c_5}{c_1^6}\right) R_{ij}^5 \\ c_1 = \frac{2}{\pi} exp[-\frac{1}{2}(\theta_i^2 + \theta_j^2)] \\ c_3 = \frac{1}{3\pi} exp[-\frac{1}{2}(\theta_i^2 + \theta_j^2)](\theta_i^2 - 1)(\theta_j^2 - 1) \\ c_5 = \frac{1}{60\pi} exp[-\frac{1}{2}(\theta_i^2 + \theta_j^2)](3 - 6\theta_i^2 + \theta_i^4)(3 - 6\theta_j^2 + \theta_j^4) \end{gathered} \tag{3}$$

where $\theta_i \triangleq \frac{v_{th_i}}{\sigma_i}$ is the normalized threshold level of channel i:

$$\theta_i = \Phi^{-1}\left(1 - \frac{\langle s_i^2 \rangle}{2}\right) \tag{4}$$

Φ^{-1} represents the inverse normal distribution cumulative density function (INCDF), which lacks a closed-form solution, and existing numerical approximation methods typically exhibit high computational complexity. This renders them challenging to implement in real-time on resource-constrained FPGA platforms.

The visibility functions are measured by the complex correlation among the pairs of antenna outputs [23]. As shown in Figure 1, the system noise temperature $Tsys_{i,j}$ is derived via the two-point noise-injection calibration method in amplitude calibration. Subsequently, the visibility functions are obtained by calibrating the correlation coefficients ρ_{ab} in accordance with (5)

 doi:10.20944/preprints202603.2178.v1

$$V_{ij} = \sqrt{Tsys_i Tsys_j}\rho_{ij} \tag{5}$$

As illustrated in Figure 1, the G-matrix inversion method is conventionally implemented in the ground processing to achieve high-accuracy TB reconstruction. However, this approach involves intensive computational overhead, particularly in handing non-ideal system responses, which precludes its feasibility for real-time onboard imaging.

For fast-view imaging scenarios, it is reasonable to assume that all antenna elements exhibit identical radiation patterns, and the influence of the fringe-washing function can be neglected. Under these conditions, the V_{ij} and T_B in (1) form a standard Fourier relationship. Once the VF is derived from (5), real-time TB reconstruction can be readily implemented in hardware (e.g., FPGA) using the IFFT. The major computational bottleneck for real-time imaging lies in the estimation of the normalized threshold level θ_i, which is required to convert the raw digital covariance R_{ij} into correlation coefficients ρ_{ij}. As indicated in (4), this procedure is equivalent to calculating INCDF, which presents substantial challenges for efficient FPGA implementation.

Furthermore, the accuracy of these calculations directly determines the final imaging accuracy. To enable real-time imaging, an INCDF estimation method must be developed that achieves an optimal balance between accuracy and computational efficiency, while maintaining hardware-friendly characteristics for practical FPGA deployment.

2.2. Real-Time Onboard RFI Localization

The onboard RFI detection shown in Figure 1 utilizes the interquartile range (IQR) method for outlier detection across total-power, cross-power, and visibility functions, followed by a voting-based decision rule to integrate distributed results and minimize the false alarm rate [11]. After onboard RFI detection is completed, the identified contaminated data are mitigated. The downlinked data lack RFI information, preventing RFI localization on the ground. Consequently, to reconstruct RFI distribution maps or facilitate advanced coordinate-based RFI excision, it is imperative to perform onboard RFI localization prior to the mitigation state.

Currently, existing ground-based RFI localization can be broadly categorized into two types. The first type operates in the spatial frequency domain, such as employing the multiple signal classification (MUSIC) algorithm for direction-of-arrival (DOA) estimation to locate RFIs [24,25]. The second type works in the spatial domain, which iteratively excises RFIs with preset intensities and positions from the original TB. The RFI location is then estimated by evaluating the characteristics of the excised TB [26,27]. Both categories of methods typically involve high computational complexity, making them unsuitable for real-time onboard implementation.

To address these challenges, this paper proposes a real-time onboard RFI localization scheme facilitated by a high-efficiency onboard TB reconstruction method.

2.3. Architecture of Real-Time Imaging and RFI Localization MIR

The architecture of the proposed three-level quantized MIR system, which features integrated onboard real-time imaging and RFI localization capabilities, is illustrated in Figure 2.

 doi:10.20944/preprints202603.2178.v1

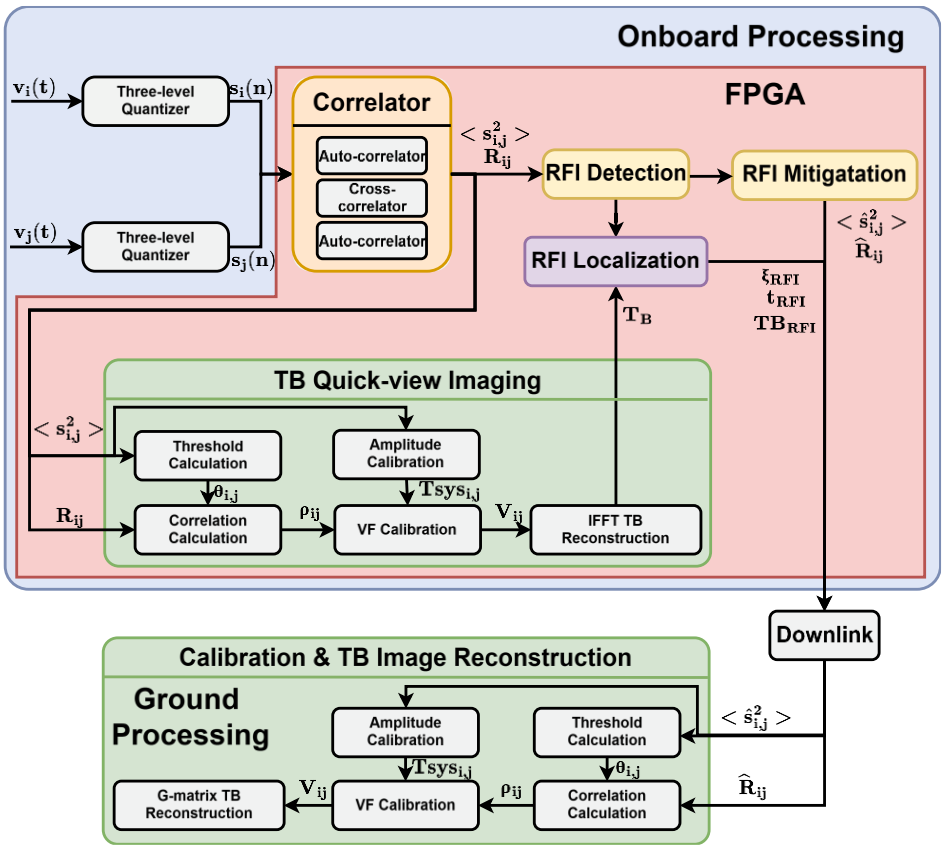

Figure 2. Architecture of three-level quantized MIR with real-time onboard imaging, RFI detection and mitigation, and RFI localization.

In contrast to the architecture shown in Figure 1, the system depicted in Figure 2 leverages real-time quantization threshold estimation and correlation coefficient calculation to enable onboard real-time TB quick-view imaging via IFFT. By accepting a manageable trade-off in imaging accuracy, this capability migrates the imaging, which was previously restricted to ground-based segments due to computational and downlink constrains, directly onto the satellite platform.

Based on the RFI detection results and the onboard real-time TB reconstruction, the RFI locator performs RFI localization. The localization information together with the RFI-mitigated data are downlinked to the ground station.

All the above procedures, including data preprocessing, TB reconstruction, RFI detection and mitigation, and RFI localization can be integrated within a single FPGA.

For real-time imaging, the error of the TB is primarily introduced by the following two components: 1) the error of the fast estimation algorithm for the normalized threshold level and 2) the quantization error introduced by data truncation when implemented in an FPGA. The two components will be discussed in Section III.

3. Hardware-Efficient Algorithms for Real-time Processing: Threshold Estimation and RFI Localization

Building upon the system architecture and theoretical constraints established in Section II, this section details the specific algorithm implementation and optimization strategies required for real-time onboard processing. As previously identified, the primary computational bottleneck for achieving real-time three-level quantized MIR imaging lies in the efficient estimation of the normalized threshold level, and high-accuracy localization of RFI within limited hardware resources. To address these challenges, Part A investigates and evaluates three rapid computation methodologies: Acklam's algorithm (AKA), polynomial fitting algorithm (PFA), and Taylor

 doi:10.20944/preprints202603.2178.v1

expansion algorithm (TEA). The impact of data bit-width and truncation errors are also analyzed to provide a hardware-efficient configuration. Part B introduces the real-time RFI localization method (RRLM), which leverages the point spread function (PSF) symmetry of the reconstructed TB to achieve sub-pixel cross-track localization accuracy.

3.1. Normalized Threshold Level Estimation Method

Real-time computation of normalized quantization threshold level (i.e., calculation of the INCDF) constitutes an essential procedure in three-level quantized MIR. The INCDF lacks a closed-form analytical solution. In non-real-time MIR imaging applications, its computation conventionally relies on ground-based numerical processing. Established techniques including rational fraction approximation, iterative optimization, and special function transformation encounter FPGA implementation challenges due to computational complexity. We therefore investigate rapid computation methodologies suitable for FPGA implementation to enable real-time TB reconstruction.

AKA uses the fact that $\Phi^{-1}(x)$ is the INCDF, then $G^{-1}(\mathrm{x})=\Phi^{-1}(x+1/2)$ is an odd function. The algorithm uses rational minimax approximation to compute θ, and is a fast and accurate algorithm proposed by Acklam for computing INCDF [28] using the following equation. The coefficients $\mathrm{a_n}, \mathrm{b_n}$ is shown in the Appendix A.

$$\theta = \Phi_{\mathrm{AKA}}^{-1}(\mathrm{x}) = \frac{(\mathrm{a_1 m^n + a_2 m^{n-1} \cdots + a_{n+1} m^0})(\mathrm{x} - 0.5)}{(\mathrm{b_1 m^n + b_2 m^{n-1} \cdots + b_n m^1 + 1})} \\ m = (x - 0.5)^2 \tag{6}$$

Given that the normalized threshold level θ is predominantly distributed within the interval [0.3,0.9], the performance evaluation is specifically concentrated on this region. As shown in Figure 3(a), AKA achieves errors below -170dB, demonstrating high computational accuracy. While implemented in an FPGA, AKA requires significant resources and time for division operations.

PFA calculates the normalized threshold level using the following polynomial. After obtaining the fitting coefficients a_n through polynomial fitting, nth-order polynomial fitting requires (n-1) addition and (n-1) multiplication operations to quickly calculate θ. This facilitates the implementation of the algorithm in an FPGA.

$$\theta = \Phi_{\mathrm{PFA}}^{-1}(\mathrm{x}) = \mathrm{a_n x^n} + \cdots \mathrm{a_2 x^2} + \mathrm{a_1 x^1} + \mathrm{a_0} \tag{7}$$

The accuracy of the PFA is influenced by factors such as the fitting interval and the order of the polynomial. Based on Figure 3(a), it can be observed that when the order of the polynomial is 2, the error is below -50dB, and within the fitting interval, the error oscillates around the maximum error. As the center point of the fitting interval and the size of the fitting region increases, the RMSE within the entire interval also increases.

TEA expands the NCDF around a point using the Taylor series, then calculates θ according to (8). The coefficients $\mathrm{a_n}$ is obtained according to [29].

$$\theta = \Phi_{TEA}^{-1}(x) = a_1 x_0 + a_2 x_0^2 + \cdots + a_n x_0^n \\ x_0 = (x - a_0) \tag{8}$$

As shown in Figure 3(a), TEA achieves low errors near the expansion point. However, as the distance from the expansion point increases, the errors rise rapidly.

 doi:10.20944/preprints202603.2178.v1

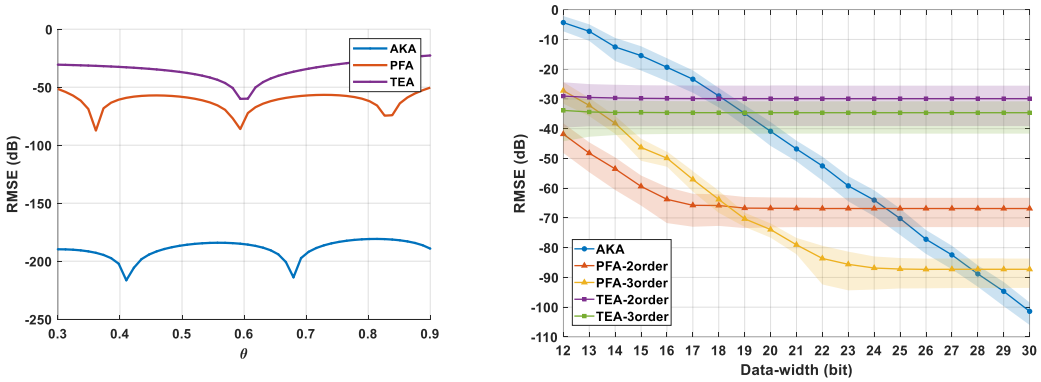

(**a**) (**b**)

Figure 3. (a) Error analysis of AKA, 2-order PFA and 2-order TEA. (b) Error analysis of three algorithms under different data-width.

While the three algorithms provide a theoretical basis for threshold estimation, their practical performance is intrinsically linked to the constraints of the hardware architecture. In FPGA implementation of real-time TB reconstruction, data truncation introduces errors during both normalized threshold level computation and TB reconstruction processes.

To quantitatively evaluate the impact of data truncation effects on the estimation accuracy across different algorithms, numerical simulations were conducted under various data bit-width. As shown in Figure 3(b), the x-axis represents the data bit-width set in the FPGA, the y-axis represents the RMSE, and the width of the bands indicates the standard deviation (STD) of the error. The error introduced by these algorithms decreases as the data bit-width increases and reaches a certain point where it no longer varies with the data bit-width. For PFA, with the same fitting interval, a larger data bit-width leads to a decrease in the RMSE with increasing order of the polynomial. When the data bit-width is smaller, higher-order polynomial fits may exhibit larger errors. This occurs because the integer part of the fitting coefficients increases with the order, while the decimal part has a smaller data bit-width, resulting in increased errors. Therefore, a larger data bit-width is required to demonstrate the high precision characteristics of higher-order polynomial fits.

The required data bit-width, logic resources, execution time, and algorithm precision for calculating one correlation coefficient for the three real-time estimation algorithms have been tested in a dedicated FPGA hardware and shown in Table 1.

Table 1. Resource Consumption of Three Algorithms in Calculating Normalized Threshold level.

Resource	AKA	PFA	TEA
Data-width(bit)	23	16	16
LUT	2785	253	253
LUTRAM	6	0	0
FF	7892	280	280
DSP	4	3	3
Time (clock cycle)	109	23	23
Time(μs)	1.09	0.23	0.23
RMSE	-63	-60	-30

The comparative data in Table 1 reveals a clear trade-off between computational overhead and estimation accuracy among the three algorithms: AKA offers superior accuracy for platform with abundant resources, while TEA provides a localized high-accuracy solution when θ is restricted to a narrow range. Notably, PFA achieves the most favorable compromise by balancing reconstruction fidelity with computational latency. Its flexible configuration and high time-efficiency make it the optimal choice for resource-constrained onboard systems requiring high-throughput real-time imaging.

 doi:10.20944/preprints202603.2178.v1

Meanwhile, the real-time normalized threshold level computation methods reduce calculation time while introducing additional errors that ultimately propagate into TB reconstruction errors. Figure 4 illustrates the relationship between TB reconstruction errors and normalized threshold level errors under varying data truncation levels through simulation. The x-axis represents the RMSE of normalized threshold levels, while the y-axis denotes the RMSE of TB. At lower data bit width, reconstruction errors are primarily dominated by truncation effects. At higher bit-widths, TB errors increase with growing normalized threshold level error inaccuracies.

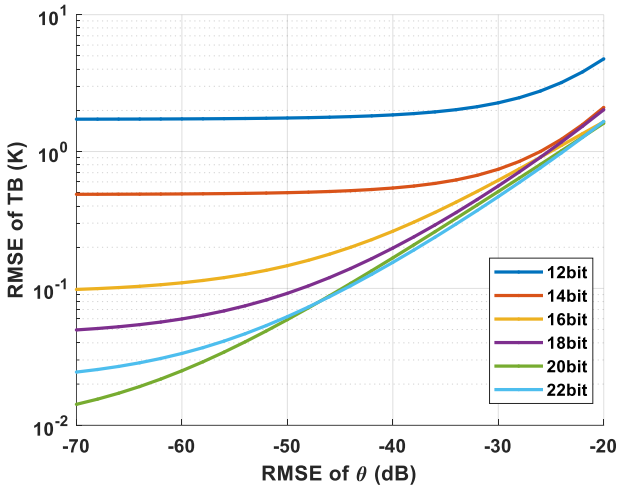

Figure 4. RMSE of brightness temperature under different normalized threshold levels' RMSE and data bit-width.

3.2. Real-Time RFI Localization Method

The one-dimensional MIR performs interferometric imaging via aperture synthesis in the cross-track direction, while employing real-aperture imaging in the along-track direction. For RFI localization, a real-time RFI localization method (RRLM) is applied to determine the RFI location in the cross-track direction. The frame-by-frame localization results are then downlinked to the ground station, where the along-track RFI locations are subsequently derived.

For RFI localization in the cross-track direction, the RFI treated as a point target. The reconstructed TB of an RFI with intensity I_{RFI} at location ξ_{RFI} is given by the following equation:

$$T_B(\xi) = \int I_{RFI} \cdot e^{j2\pi(\xi-\xi_{RFI})} du \tag{9}$$

The RRLM utilizes the symmetry of the reconstructed TB for a point target, as shown in the following equation, to achieve RFI location:

$$T_B\left(\xi_{RFI} - \Delta\xi\right) = T_B\left(\xi_{RFI} + \Delta\xi\right) \tag{10}$$

where ξ_{RFI} represents the location of RFI. When $\Delta\xi$ is smaller than the system spatial resolution, the TB remains identical on both sides of the RFI.

Based on the aforementioned characteristics, a high-precision RRLM is designed. The algorithm procedure is as follows:

Algorithm 1: Real-time RFI Localization Method (RRLM)

Input: $T_B(\xi)$, ξ_{shift}, $T_{B_{threshold}}$, V_{ij}

Output: ξ_{RFI}

Coarse Estimation:

Estimate ξ_{RFI_0} using the peak amplitude of $T_B(\xi)$

$\xi_{RFI_0} \leftarrow arg\ max_{\xi}|T_B(\xi)|$

 doi:10.20944/preprints202603.2178.v1

Fine Localization

Initialize $\xi_{shift} \leftarrow 0,\ n \leftarrow 0$

$T_{B_{left}} \leftarrow T_B(\xi_{RFI_0} - \Delta\xi), T_{B_{right}} \leftarrow T_B(\xi_{RFI_0} + \Delta\xi)$

While $|T_{B_{left}} - T_{B_{right}}| \leq T_{B_{threshold}}$ **do**

Compute T_B at symmetric points via IDFT of V_{ij}:

$T_{B_{left}} \leftarrow T_B(\xi_{RFI_0} - \Delta\xi + \xi_{shift})$

$T_{B_{right}} \leftarrow T_B(\xi_{RFI_0} + \Delta\xi + \xi_{shift})$

$n \leftarrow n + 1$

If $T_{B_{left}} > T_{B_{right}}$

$\xi_{shift} \leftarrow -\frac{2\Delta\xi}{2^n}$

Else

$\xi_{shift} \leftarrow \frac{2\Delta\xi}{2^n}$

End If

End While

$\xi_{RFI} \leftarrow \xi_{RFI_0} + \xi_{shift}$

Return ξ_{RFI}

The localization accuracy and spatial resolution of the proposed RRLM are validated through a dedicated simulation framework. To maintain practical relevance for spaceborne remote sensing, a satellite Earth observation scenario from an orbital altitude of 800km is simulated to evaluate performance across varying spatial resolution.

To quantify the RRLM localization capability, a series of RFIs with fixed intensity and random locations are set, and the localization error is obtained via Monte Carlo simulation. Figure 5(a) illustrates the localization error as a percentage of the spatial resolution against varying RFI intensities. It is observed that the error ratio initially scales with RFI intensity before exhibiting an asymptotic stabilization. Notably, systems with finer spatial resolution consistently yield smaller relative localization errors, signifying enhanced accuracy.

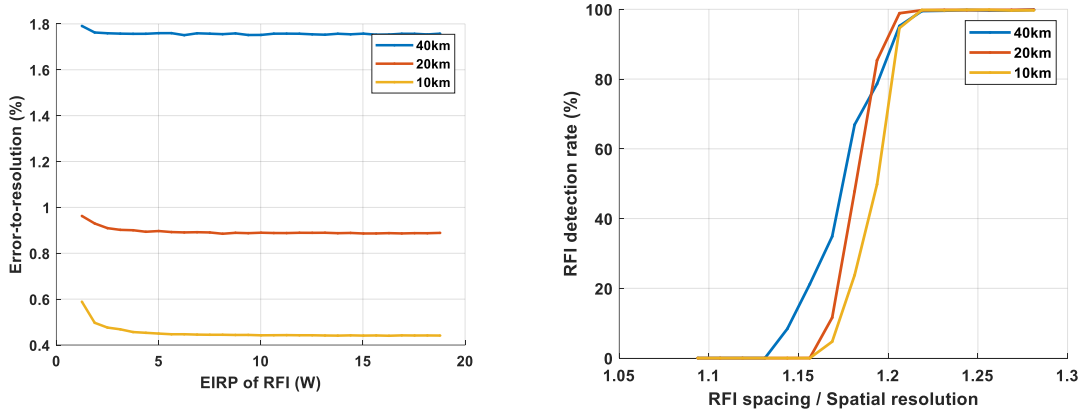

(**a**) (**b**)

Figure 5. (a)Localization capability and (b)spatial resolution of the RRLM.

The high accuracy of RRLM is fundamentally rooted in the exploitation of the PSF symmetry. The localization process essentially performs a refined search near the PSF peak by varying the reconstructed TB positions. Analytically, the localization capability is governed by the inverse of the PSF slope, defined as the rate of the direction cosine relative to the reconstructed TB in the peak vicinity. This inverse slope-to-resolution ratio varies linearly with the spatial resolution. Specifically, a linear increase in spatial resolution leads to a proportional decrease in this ratio, resulting in the linear reduction of the localization error observed in Figure 5(a).

 doi:10.20944/preprints202603.2178.v1

Finally, the spatial resolution of the RRLM was evaluated via Monte Carlo simulations involving two RFIs with random intensities at fixed inter-source spacings. The detection rate, plotted in Figure 5(b) against the spacing-to-resolution ratio, serves as the metric for spatial resolution. As the separation increases, the detection rate rises monotonically from zero, stabilizing near 100%. These simulation results confirm that the RRLM can effectively distinguish and localize dual RFI sources once their spatial separation exceeds 1.23 times the system's spatial resolution.

4. Experiments

This section presents two experiments conducted with two 1D-MIRs to validate real-time TB reconstructed and real-time RFI localization, respectively. The system parameters of these two MIRs are listed in the following table.

Table 2. System parameters of two 1D-MIRs.

Specification	Real-time Imaging MIR	Real-time RFI location MIR
Frequency	50GHz	1.4GHz
Bandwidth	320MHz	25MHz
Number of receivers	15	5
Spatial resolution	1.43°	15°
Sensitivity	0.5K@25ms	0.1K@1s

4.1. Real-Time Imaging Experiment

Real-time imaging experiments have been carried out with a one-dimensional MIR prototype comprises 15 antenna elements configured in large minimum redundancy linear array [30], forming 159 baselines. As shown in Figure 6, the prototype is mounted on a pedestrian bridge above an expressway to observe passing vehicles. The real aperture direction is aligned with the direction of vehicle travel, while the synthetic aperture direction is perpendicular to the direction of vehicle travel. The prototype remains stationary, and imaging is achieved through the movement of the vehicles. 2nd order PFA with 16-bit data width has been selected and implemented in the TB Quick-view Imaging of the prototype, aligned with the architecture illustrated in Figure 2. The raw correlation counts have also been output for algorithm verification.

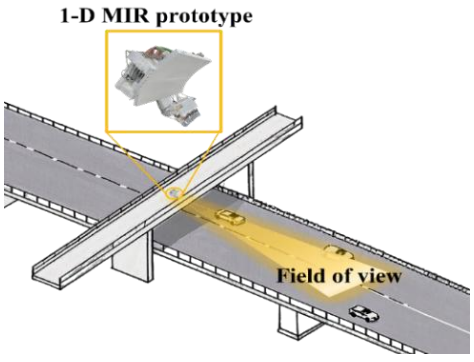

Figure 6. Experimental scene.

Figure 7 illustrates the experimental results. The real-time TB image in Figure 7(b) is in good agreement with the actual targeting scene in Figure 7(a). The total real-time imaging processing time is 570.9μs when system clock is 100MHz. Two offline reference imaging tests have been carried out with the raw correlation counts, one of which is standard image reconstruction with accurate numerical calculation of INCDF, the other is image reconstruction with 2nd order FPA without data truncation. The standard reconstructed TB is used as a benchmark, to evaluate the errors introduced by PFA and bit- truncation. Figure 7(c) illustrates the difference between the real-time reconstructed

 doi:10.20944/preprints202603.2178.v1

TB (2nd order PFA with 16-bit data width) and the benchmark TB, while Figure 7(d) shows the difference between the tested reconstructed TB (2nd order PFA without data truncation) and benchmark TB. Figure 7(e) and (f) show their corresponding probability density distribution, in which purple bar charts represent statistical characteristics (mean and standard deviation) of the TB error, red curves represent the kernel density estimation (KDE) of TB error, and blue curves denote the theoretical probability density function (PDF) of a Gaussian distribution with same mean and standard deviation values as the values in purple charts. It can be seen that, in both cases the statistical properties of the TB errors are highly consistent with zero-mean Gaussian distribution. Data truncation contributes most of the real-time imaging TB error. The TB error purely introduced by PFA, as illustrated in Figure 7(d) and (f), are almost negligible (standard deviation is only 0.008K), but the error pattern shows some correlation with the target TB distribution.

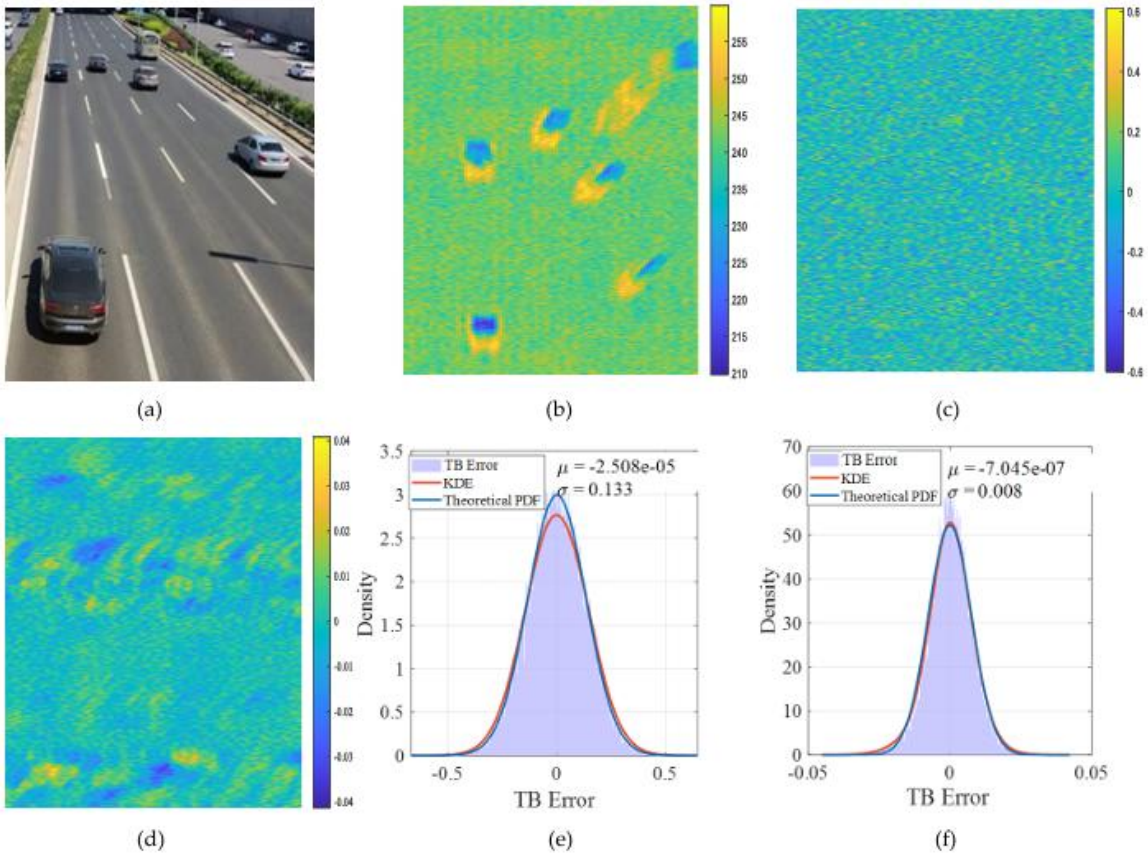

Figure 7. Real-time Imaging Experiment results; (a) Targeting Scene; (b) Real-time Reconstructed TB through PFA in FPGA; (c) TB error of PFA in FPGA; (d) TB error of PFA without data truncation; (e) Probability density distribution of (c); (f) Probability density distribution of (d).

For the practical real-time PFA implementation in FPGA with 16-bit data width, the TB error of 0.133K standard deviation is dominated by data truncation effects. This result very well aligns with Figure 4: when the RMSE of normalized threshold level is -60dB and data bit-width is 16, the RMSE of reconstructed TB is approximately -16.9dB ($10^{-16.9/20}$≈0.142).

Given that the error in the visibility function satisfies the Central Limit Theorem, the brightness temperature reconstruction error after IFFT follows a Gaussian distribution. 1) Independence: When the data bit-width is sufficiently large (exceeding 8 bits), truncation-induced errors in the visibility function can be approximated as independently distributed. 2) Identical Distribution: Under stationary statistical characteristics and uniform quantization, the error distribution remains identical across all sample points.

 doi:10.20944/preprints202603.2178.v1

4.2. Real-Time RFI Localization Experiment

To validate the practical localization performance of the proposed RRLM algorithm, an airborne flight experiment was conducted using a 1-D L-band MIR [31]. The architecture of this MIR system is depicted in Figure 2, with its primary instrument parameters summarized in Table 2, featuring a nominal spatial resolution of 15°.

The experiment was carried out over Yantai, Shandong Province, China. Figure 8(c) presents the reconstructed TB with a 1-s integration time after RFI mitigation, corresponding to the correlation data downlinked to the ground station as illustrated in the system diagram of Figure 2. In contrast, Figure 8(a) displays the 1-s integrated TB without mitigation. It is evident that the RFI has been effectively suppressed, and the TB has restored its normal geographic observation characteristics. RFI detection and localization are performed on the 10-ms integrated data frames shown in Figure 8(b). In the unmitigated 10-ms TB, the RFI exhibit prominent PSF features, which provides the physical basis for the RRLM algorithm to achieve accurate localization by exploring PFS symmetry. Upon detection of RFI within the 10-ms data, the RFI locator determines the source coordinates through real-time imaging following the RRLM algorithm. Only the RFI localization data and the mitigated 1-s integrated data are downlinked, while the raw unmitigated data frames shown in Figure 8(a) and (b) are not transmitted to the ground station.

To evaluate the localization accuracy of RRLM, its results were compared with the MUSIC algorithm. Figure 8(d) displays the comparison between RRLM and MUSIC localization results across 100 consecutive 10-ms data frames. The findings indicate that the RRLM results are in high agreement with those of the MUSIC algorithm. Statistical analysis shows that the average localization error of RRLM is 0.32°, representing only 2.1% of the system spatial resolution. This performance concurs with theoretical analysis and validates the localization capability of RRLM.

This experiment demonstrates that the RRLM, running on a resource-constrained FPGA platform, successfully retrieves RFI spatial information via real-time imaging before data excision occurs. This addresses the critical limitation of current spaceborne systems, where RFI positional information is lost after onboard mitigation, thereby providing technical support for the subsequent generation of global RFI statistical distribution maps.

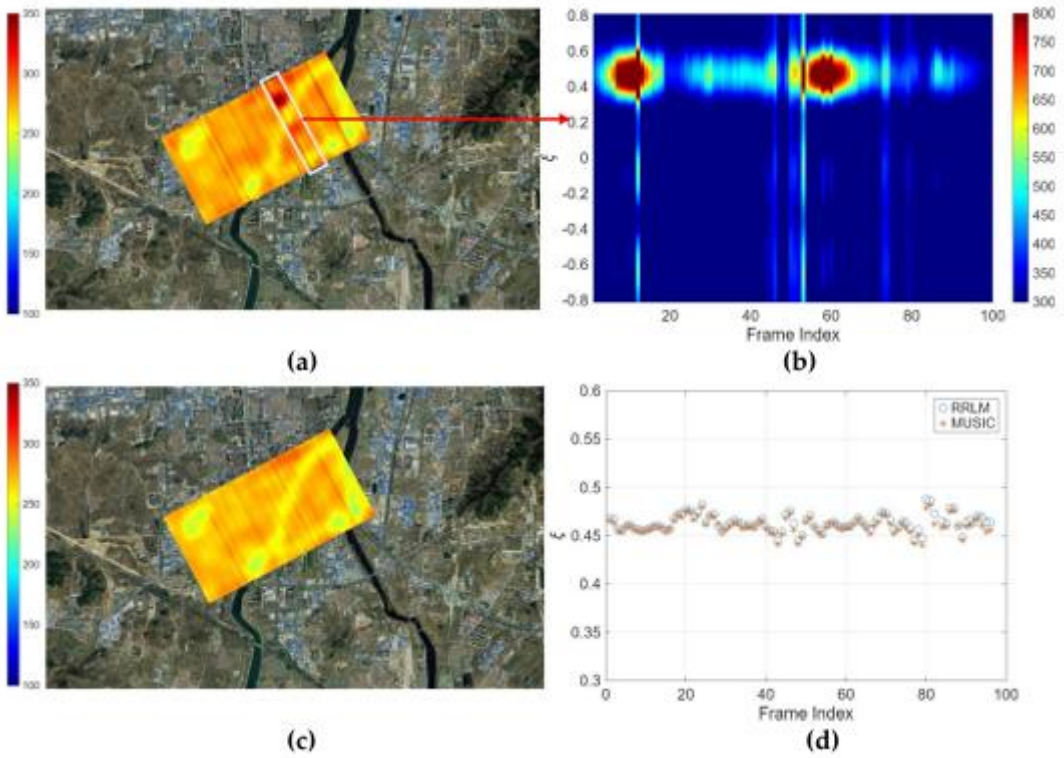

 doi:10.20944/preprints202603.2178.v1

Figure 8. Cross-track RFI real-time localization experiment. (a) TB before RFI mitigation; (b) TB in the RFI-affected region under a 10ms integration time (note: the 10ms integration data are for testing purposes only). (c) TB after RFI mitigation; (d) RFI localization results of RRLM and MUSIC.

5. Conclusions

This article presents three methods for real-time calculation of three-level quantization normalized threshold level to achieve real-time passive microwave interferometric imaging. We can choose the appropriate algorithm and data bit-width based on the error requirements to save logical resources and time. For one-dimensional MIR with 159 baselines, the brightness temperature reconstruction takes only 570.9μs, with a reconstruction error distributed as N(-2.508e-5,0.1332). This performance significantly facilitates onboard RFI localization: for a 1-D MIR with a spatial resolution of 15°, the RFI localization error remains below 2.1% of the spatial resolution. In the future, we will conduct research on real-time calibration methods to further improve the inversion accuracy and explore real-time imaging methods for two-dimensional MIR.

Appendix A Coefficients of AKA

The coefficients a_n, b_n employed in the AKA are provided in the following table.

Table A1. Coefficients of AKA.

Coefficient	Value	Coefficient	Value
a_1	-3.969683028665376e+01	b_1	-5.447609879822406e+01
a_2	2.209460984245205e+02	b_2	1.615858368580409e+02
a_3	-2.759285104469687e+02	b_3	-1.556989798598866e+02
a_4	1.383577518672690e+02	b_4	6.680131188771972e+01
a_5	-3.066479806614716e+01	b_5	-1.328068155288572e+01
a_6	2.506628277459239e+00		-5.447609879822406e+01

References

1. Martín-Neira, M.; LeVine, D.M.; Kerr, Y.; Skou, N.; Peichl, M.; Camps, A.; Corbella, I.; Hallikainen, M.; Font, J.; Wu, J.; et al. Microwave Interferometric Radiometry in Remote Sensing: An Invited Historical Review: MICROWAVE INTERFEROMETRIC RADIOMETRY. Radio Sci. 2014, 49, 415–449, doi:10.1002/2013RS005230.
2. Hagen, J.B.; Farley, D.T. Digital-Correlation Techniques in Radio Science. Radio Sci. 1973, 8, 775–784, doi:10.1029/RS008i008p00775.
3. Liu, J.; Han, D.; Guo, X.; Niu, L.; Liu, H. Characterization Method for Digital Correlator of Interferometric Radiometers Based on Correlated Noise Source. IEEE Geosci. Remote Sens. Lett. 2023, 20, 1–5, doi:10.1109/LGRS.2023.3299292.
4. Corbella, I.; Torres, F.; Camps, A.; Colliander, A.; Martin-Neira, M.; Ribo, S.; Rautiainen, K.; Duffo, N.; Vall-llossera, M. MIRAS End-to-End Calibration: Application to SMOS L1 Processor. IEEE Trans. Geosci. Remote Sens. 2005, 43, 1126–1134, doi:10.1109/TGRS.2004.840458.
5. Kulkarni; S; R; Heiles; C How to Obtain the True Correlation from a 3-Level Digital Correlator. Astron. J. 1980, 85, 1413–1413.
6. Cheng Zhang; Hao Liu; Ji Wu; Shengwei Zhang; Jingye Yan; Lijie Niu; Weiying Sun; Huiling Li Imaging Analysis and First Results of the Geostationary Interferometric Microwave Sounder Demonstrator. IEEE Trans. Geosci. Remote Sens. 2015, 53, 207–218, doi:10.1109/TGRS.2014.2320983.
7. Piepmeier, J.R.; Gasiewski, A.J. Digital Correlation Microwave Polarimetry: Analysis and Demonstration. IEEE Trans. Geosci. Remote Sens. 2001, 39, 2392–2410, doi:10.1109/36.964976.
8. Gao, G.; Yao, L.; Li, W.; Zhang, L.; Zhang, M. Onboard Information Fusion for Multisatellite Collaborative Observation: Summary, Challenges, and Perspectives. IEEE Geosci. Remote Sens. Mag. 2023, 11, 40–59, doi:10.1109/MGRS.2023.3274301.

 doi:10.20944/preprints202603.2178.v1

9. Misra, S.; Kocz, J.; Jarnot, R.; Brown, S.T.; Bendig, R.; Felten, C.; Johnson, J.T. Development of an On-Board Wide-Band Processor for Radio Frequency Interference Detection and Filtering. IEEE Trans. Geosci. Remote Sens. 2019, 57, 3191–3203, doi:10.1109/TGRS.2018.2882306.
10. Johnson, J.T.; Ball, C.; Chen, C.-C.; McKelvey, C.; Smith, G.E.; Andrews, M.; O'Brien, A.; Garry, J.L.; Misra, S.; Bendig, R.; et al. Real-Time Detection and Filtering of Radio Frequency Interference Onboard a Spaceborne Microwave Radiometer: The CubeRRT Mission. IEEE J. Sel. Top. Appl. Earth Obs. Remote Sens. 2020, 13, 1610–1624, doi:10.1109/JSTARS.2020.2978016.
11. Guo, T.; Guo, X.; Liu, H.; Han, D.; Zhang, C.; Huo, C.; Tang, Y.; Niu, L.; Li, G.; Wu, J. Study of the Real-Time Onboard Radio Frequency Interference Detection and Mitigation Strategy for MICAP L-Band Radiometer. IEEE Trans. Geosci. Remote Sens. 2022, 60, 1–14, doi:10.1109/TGRS.2022.3205963.
12. Perez-Portero, A.; Querol, J.; Camps, A. Resource-Efficient FPGA Architecture for Real-Time RFI Mitigation in Interferometric Radiometers. Sensors 2024, 24, 8001, doi:10.3390/s24248001.
13. Kristensen, S.S.; Balling, J.E.; Sobjarg, S.S.; Skou, N. On-Board Radio Frequency Interference Processor for the Copernicus Imaging Microwave Radiometer. In Proceedings of the IGARSS 2022 - 2022 IEEE International Geoscience and Remote Sensing Symposium; IEEE: Kuala Lumpur, Malaysia, July 17 2022; pp. 5266–5269.
14. Piepmeier, J.R.; Johnson, J.T.; Mohammed, P.N.; Bradley, D.; Ruf, C.; Aksoy, M.; Garcia, R.; Hudson, D.; Miles, L.; Wong, M. Radio-Frequency Interference Mitigation for the Soil Moisture Active Passive Microwave Radiometer. *IEEE Trans. Geosci. Remote Sens.* **2014**, *52*, 761–775, doi:10.1109/TGRS.2013.2281266.
15. Johnson, J.T.; Chen, C.C.; O'Brien, A.; Smith, G.E.; McKelvey, C.; Andrews, M.; Ball, C.; Misra, S.; Brown, S.; Kocz, J.; et al. The CubeSat Radiometer Radio Frequency Interference Technology Validation (CubeRRT) Mission. In Proceedings of the 2016 IEEE International Geoscience and Remote Sensing Symposium (IGARSS); IEEE: Beijing, China, July 2016; pp. 299–301.
16. Backus, B.; De Matthaeis, P.; Balague, R.O.; Díez-García, R. An IEEE Standard for Radio Frequency Interference Degradation in Microwave Remote Sensing Measurements: Technical Implications and Ongoing Efforts [Technical Committees]. IEEE Geosci. Remote Sens. Mag. 2025, 13, 463–468, doi:10.1109/MGRS.2025.3593483.
17. Appleby, R.; Robertson, D.A.; Wikner, D. Millimeter Wave Imaging: A Historical Review. In Proceedings of the Passive and Active Millimeter-Wave Imaging XX; SPIE, May 11 2017; Vol. 10189, p. 1018902.
18. Dillon, T.E.; Schuetz, C.A.; Martin, R.D.; Mackrides, D.G.; Shi, S.; Yao, P.; Shreve, K.; Harrity, C.; Prather, D.W. Passive, Real-Time Millimeter Wave Imaging for Degraded Visual Environment Mitigation. In Proceedings of the Degraded Visual Environments: Enhanced, Synthetic, and External Vision Solutions 2015; SPIE, May 21 2015; Vol. 9471, pp. 10–18.
19. Ahmed, S.S. Microwave Imaging in Security — Two Decades of Innovation. IEEE J. Microw. 2021, 1, 191–201, doi:10.1109/JMW.2020.3035790.
20. Feng, H.; An, D.; Tu, H.; Bu, W.; Wang, W.; Zhang, Y.; Zhang, H.; Meng, X.; Wei, W.; Gao, B.; et al. A Passive Video-Rate Terahertz Human Body Imager with Real-Time Calibration for Security Applications. Appl. Phys. B 2020, 126, 143, doi:10.1007/s00340-020-07496-3.
21. Salmon, N.A.; Macpherson, R.; Harvey, A.; Hall, P.; Hayward, S.; Wilkinson, P.; Taylor, C. First Video Rate Imagery from a 32-Channel 22-GHz Aperture Synthesis Passive Millimetre Wave Imager.; Krapels, K.A., Salmon, N.A., Jacobs, E., Eds.; Prague, Czech Republic, October 6 2011; p. 818805.
22. Corbella, I.; Duffo, N.; Vall-llossera, M.; Camps, A.; Torres, F. The Visibility Function in Interferometric Aperture Synthesis Radiometry. IEEE Trans. Geosci. Remote Sens. 2004, 42, 1677–1682, doi:10.1109/TGRS.2004.830641.
23. Corbella, I.; Torres, F.; Camps, A.; Colliander, A.; Martin-Neira, M.; Ribo, S.; Rautiainen, K.; Duffo, N.; Vall-llossera, M. MIRAS End-to-End Calibration: Application to SMOS L1 Processor. IEEE Trans. Geosci. Remote Sens. 2005, 43, 1126–1134, doi:10.1109/TGRS.2004.840458.
24. Camps, A.; Gourrion, J.; Tarongi, J.M.; Vall Llossera, M.; Gutierrez, A.; Barbosa, J.; Castro, R. Radio-Frequency Interference Detection and Mitigation Algorithms for Synthetic Aperture Radiometers. Algorithms 2011, 4, 155–182, doi:10.3390/a4030155.

 doi:10.20944/preprints202603.2178.v1

25. Anterrieu, E.; Khazaal, A.; Cabot, F.; Kerr, Y. Geolocation of RFI Sources with Sub-Kilometric Accuracy from SMOS Interferometric Data. Remote Sens. Environ. 2016, 180, 76–84, doi:10.1016/j.rse.2016.02.007.
26. Park, H.; Gonzalez-Gambau, V.; Camps, A. High Angular Resolution RFI Localization in Synthetic Aperture Interferometric Radiometers Using Direction-of-Arrival Estimation. IEEE Geosci. Remote Sens. Lett. 2015, 12, 102–106, doi:10.1109/LGRS.2014.2327006.
27. Park, H.; Gonzalez-Gambau, V.; Camps, A.; Vall-llossera, M. Improved MUSIC-Based SMOS RFI Source Detection and Geolocation Algorithm. IEEE Trans. Geosci. Remote Sens. 2016, 54, 1311–1322, doi:10.1109/TGRS.2015.2477435.
28. An algorithm for computing the inverse normal cumulative distribution function. Available online. Available: http: //stackedboxes.org/2017/05/01/acklams-normal-quantile-function/
29. Abramowitz, M.; Stegun, I.A. Handbook of Mathmatical Functions; 9th ed.; Dover: New York, 1964;
30. Schwartau, F.; Schröder, Y.; Wolf, L.; Schoebel, J. Large Minimum Redundancy Linear Arrays: Systematic Search of Perfect and Optimal Rulers Exploiting Parallel Processing. IEEE Open J. Antennas Propag. 2021, 2, 79–85, doi:10.1109/ojap.2020.3043541.
31. Li, B.; Guo, X.; Liu, H.; Han, D.; Tong, X.; Zhang, C.; Niu, L.; Li, G.; Zhou, W. MICAP Radiometer Airborne Campaign: Preliminary Results of L/C/K Tri-Frequency Interferometric Radiometer. In Proceedings of the IGARSS 2024 - 2024 IEEE International Geoscience and Remote Sensing Symposium; IEEE: Athens, Greece, July 7 2024; pp. 6713–6716.